Nano-Micro Letters

e-ISSN 2150-5551
CN 31-2103/TB

ARTICLE

https://doi.org/10.1007/s40820-022-00948-9

Cite as
Nano-Micro Lett.
(2022) 14:208

Received: 21 July 2022
Accepted: 19 September 2022
Published online: 26 October 2022

Iodine Promoted Ultralow Zn Nucleation Overpotential and Zn-Rich Cathode for Low-Cost, Fast-Production and High-Energy Density Anode-Free Zn-Iodine Batteries

Yixiang Zhang[1], Lequan Wang[1], Qingyun Li[1], Bo Hu[1], Junming Kang[1], Yuhuan Meng[1], Zedong Zhao[1] ✉, Hongbin Lu[1,2] ✉

HIGHLIGHTS

- The I_3^- additive promoted in situ formation of zincophilic Cu nanoclusters on commercial Cu foil, which achieves uniform Zn deposition with ultralow nucleation overpotential and high reversibility.
- The Zn-rich ZnI_2 cathode confined by graphene/polyvinyl pyrrolidone heterostructure shows enhanced conductivity and shuttle effect suppression, providing sufficient Zn^{2+} for the anode stably.
- The assembled anode-free Zn-iodine battery exhibits attractive features for commercialization: low cost, fast production, significantly increased energy density and durable cycle stability under practical application conditions.

ABSTRACT The anode-free design is a promising strategy to increase the energy density of aqueous Zn metal batteries (AZMBs). However, the scarcity of Zn-rich cathodes and the rapid loss of limited Zn greatly hinder their commercial applications. To address these issues, a novel anode-free Zn-iodine battery (AFZIB) was designed via a simple, low-cost and scalable approach. Iodine plays bifunctional roles in improving the AFZIB overall performance: enabling high-performance Zn-rich cathode and modulating Zn deposition behavior. On the cathode side, the ZnI_2 serves as Zn-rich cathode material. The graphene/polyvinyl pyrrolidone heterostructure was employed as an efficient host for ZnI_2 to enhance electron conductivity and suppress the shuttle effect of iodine species. On the anode side, trace I_3^- additive in the electrolyte creates surface reconstruction on the commercial Cu foil. The in situ formed zincophilic Cu nanocluster allows ultralow-overpotential and uniform Zn deposition and superior reversibility (average coulombic efficiency > 99.91% over 7,000 cycles). Based on such a configuration, AFZIB exhibits significantly increased energy density (162 Wh kg^{-1}) and durable cycle stability (63.8% capacity retention after 200 cycles) under practical application conditions. Considering the low cost and simple preparation methods of the electrode materials, this work paves the way for the practical application of AZMBs.

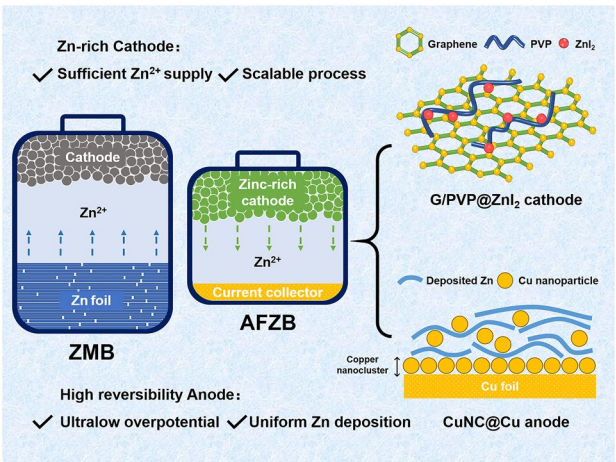

KEYWORDS Zn metal battery; Zn deposition; Zn-rich cathode; Anode-free; Energy density

✉ Zedong Zhao, 17110440016@fudan.edu.cn; Hongbin Lu, hongbinlu@fudan.edu.cn
[1] State Key Laboratory of Molecular Engineering of Polymers, Department of Macromolecular Science, Fudan University, 2005 Songhu Road, Shanghai 200438, People's Republic of China
[2] Yiwu Research Institute of Fudan University, Chengbei Road, Yiwu City, Zhejiang 322000, People's Republic of China

1 Introduction

Subject to the safety and limited availability of lithium metal [1], researchers have increasingly focused on the development of new battery systems, such as sodium, potassium, zinc, and magnesium batteries. Among them, rechargeable Zn metal batteries (RZMBs) exhibit excellent safety with their unique aqueous electrolyte, while combining low cost and high specific capacity [2]. These advantages make RZMBs an important complement to lithium batteries, especially in the field of large-scale energy storage [3]. Although the performance of RZMBs has been greatly improved, the instability [4] of the Zn anodes is still the bottleneck restricting their commercialization [5, 6]. One of the important and unresolved issues is that previous reports generally use thick Zn foils (> 100 μm) as the anode [7], which leads to high negative to positive capacity ratios (N/P > 50) [8]. The large excess of Zn can compensate for the rapid loss of Zn during cycling to achieve excellent cell performance [9]. Nevertheless, these performances cannot be used as references for practical applications because the imbalanced N/P ratio will greatly limit the actual energy density of RZMBs [10]. Therefore, achieving RZMBs with low N/P ratio is critical to advancing practical progress.

As a hostless anode, the thinner Zn foil tends to fragment and pulverize during deep discharge process, resulting in severe surface corrosion and even forming isolated dead Zn [11]. Due to the limited amount of Zn, the thin Zn foil (10 μm) cannot release its theoretical capacity upon cycling, thus it is difficult to match the cathode capacity to assemble a low N/P ratio full cell. In current studies, low N/P ratios are controlled by electrochemically pre-depositing limited Zn on conductive substrates [12]. Such a costly and complex process is only suitable for laboratory-level studies. A more promising strategy is the anode-free Zn batteries (AFZBs) [13]. The Zn-rich cathode materials serve as the Zn source, and the Zn metal anode is replaced by a deposition substrate [14]. Due to the absence of Zn foils, this strategy maximizes the energy density of the battery.

However, achieving high-performance AFZBs is more challenging. On the anode side, because there is no excess Zn, corrosion, dendrites and side reactions [15] would lead to large amounts of Zn loss and accelerate capacity degradation. As a result, the AFZBs demonstrate a very short cycle life [10]. Therefore, suppressing Zn loss and improving the Coulombic efficiency (CE) of Zn deposition/dissolution are the keys to prolonging battery lifespan. In the current research works of AFZBs, Cui et al. introduced carbon disks on the copper (Cu) substrate as uniform nucleation sites for Zn, achieving a CE as high as 99.6% [16] in the 3 M $Zn(CF_3SO_3)_2$ electrolyte. Feng et al. employed a silver-coated Cu substrate and 3 M $Zn(TFSI)_2$ electrolyte to achieve a CE of 99.86% [17]. However, the expensive electrolytes and complex electrode processes used in these efforts greatly increase the cost of full cells, which reduces the commercialization potential of AFZBs. Therefore, it is necessary to further explore low-cost, scalable methods to improve Zn deposition/dissolution CE.

On the cathode side, unlike various types of Li-rich cathodes [18], such as lithium iron phosphate ($LiFePO_4$), lithium manganate ($LiMn_2O_4$) and lithium cobaltate ($LiCoO_2$), there are few reported high-performance Zn-rich cathodes [19]. For example, the Zn manganate ($ZnMn_2O_4$) cathode possesses a complete spinel structure, resulting in slow kinetics of Zn^{2+} extraction, poor reversibility and low specific capacity [20]; the $ZnCo_2O_4$ cathode is unstable in aqueous electrolytes and requires appropriate lattice modification (e.g., Al insertion [21]) to improve its stability. Furthermore, in some AFZB studies, Zn-rich manganese cathodes were obtained by pre-zincificated β-MnO_2 [16], but such a complex and unstable procedure is unsuitable to scale up in practical applications. In this context, Zn-rich cathodes with stable Zn^{2+} supply and simple processes are urgently needed for the development of AFZBs.

Herein, from the perspective of overcoming both the cathode and anode issues of AFZBs, we report a novel, low-cost, scale-up concept to design anode-free Zn-iodine battery (AFZIB) with high energy density and long lifespan (Fig. 1). On the cathode side, we propose a ZnI_2 cathode and design a unique graphene/polyvinyl pyrrolidone (G/PVP) heterostructure as the host. PVP can effectively inhibit the shuttle effect of iodine species, while G can enhance the electronic conductivity and structure stability. Therefore, the G/PVP@ZnI_2 cathode can deliver high specific capacity (146.1 mAh g^{-1}_{ZnI2} at 1 A g^{-1}, all the specific capacities are based on the mass of ZnI_2) and excellent cycling performance (80% capacity retention after 1,000 cycles at 1 A g^{-1}). On the anode side, we employed Cu foil as the deposition substrate and added a trace amount of I_3^- (10 mM) to the electrolyte, which reacted with Cu surface to produce copper iodide (CuI). The CuI was reduced and reconstructed into Cu nanoclusters (CuNC) via

 https://doi.org/10.1007/s40820-022-00948-9

in situ electrochemical reduction, which can modulate the Zn deposition behavior with ultralow nucleation overpotential and uniform morphology. The CE is ultra-high and stable with an average value > 99.91% for 7,000 cycles. Due to the multiple functions of iodine at both cathodes and anodes, the AFZIB exhibits excellent cycle stability (capacity retention rate of 63.8% after 200 cycles) and high specific capacity (125.7 mAh g^{-1} at 1 A g^{-1}). More importantly, based on practical application level, the energy density of our AFZIB is significantly improved (162 Wh kg^{-1}, based on active material), compared to traditional ZIBs (15 Wh kg^{-1} with a N/P of 50).

2 Experimental Section

2.1 Preparation of G/PVP@ZnI_2 Cathode

The G was prepared according to our previously reported method [22]. For the G/PVP@ZnI_2 cathode fabrication, the ZnI_2, G, PVP (with an average molecular weight of 20,000) and polytetrafluoroethylene (PTFE) were mixed in ethanol at a mass ratio of 5:2:2:1 and ultrasonic dispersion for 30 min, followed by compressing onto a Ti grid. The electrodes were dried at 60 ℃ for 1 h and then punched into disks. The mass loadings of active materials were around 4–5 mg cm^{-2}. The G@ZnI_2 cathode was prepared by the same method with ZnI_2, G and PTFE ratio of 5:4:1.

2.2 Electrochemical Measurements

The I_3^- containing electrolyte (10 mM) was prepared by adding 5 mM ZnI_2 and 10 mM I_2 into the 2 M $ZnSO_4$ electrolyte. During the battery assembly process, the I_3^- containing electrolyte first contacted and fully reacted with the commercial Cu foil before loading the Zn foil.

All the batteries were assembled with 2016-coin cells, and the separator was the glass fiber diaphragm (100 μm, Whatman GF/A) with an electrolyte addition of 70 μL (if not otherwise specified). Galvanostatic discharging/charging tests were performed on the Land battery tester (CT2001A) at various current densities. The cyclic voltammetry (CV) measurements were performed on a CHI660E electrochemical workstation.

2.3 Material Characterizations

The structure and morphology of materials were characterized by field-emission scanning electron microscope (FESEM, Ultra 55). The crystal structure was measured with an X-ray diffractometer (XRD) model of PAN alytial X'Pert PRO. X-ray photoelectron spectroscopy (XPS) was measured using AXIS ULTRA DLD to obtain the surface chemical state of materials. The UV absorption spectra were measured on a Lambda750 UV–vis spectrophotometer.

3 Results and Discussion

3.1 In situ Surface Reconstruction of Cu Foil

As a low-cost and stable current collector for commercial lithium-ion batteries, Cu foil is also considered an ideal deposition substrate for Zn anodes in ZMBs [23]. For example, the recently reported Cu nanowires [24] or carbon fibers doped with Cu nanoboxes [12] show highly zincophilic features, which achieves uniform Zn deposition [25] with high CE. However, the finely designed Cu nanostructures in these efforts often require high costs and complex synthesis processes, such as the hydrothermal method [24] or high-temperature calcination [12]. Inspired by the previously reported study that employed I_3^- to suppress hydrogen evolution of Zn anodes [26], we thus propose to use I_3^- electrolyte additive to obtain zincophilic Cu nanocluster structures on the surface of commercial Cu foils via a simple in situ electrochemical reduction approach. The surface reconstruction process is simple and fast. Firstly, a trace amount of I_3^- ions (10 mM) was added to the 2 M $ZnSO_4$ aqueous electrolyte. Due to the strong oxidizing properties of I_3^-, the Cu foil reacted with the I_3^- rapidly to produce CuI on its surface. Figure 2a, d shows the in situ reaction process between I_3^- and Cu foil during the cell assembly process. After adding electrolyte to the separator (the separator ensures the uniform reaction between I_3^- and Cu foil surface), the rufous electrolyte faded within 5 min, corresponding to the color change from pink to purplish red on the surface of the Cu foil. In the XRD pattern of the iodine-treated Cu foil (Fig. 2b), the characteristic peaks at 25.4° and 42.3° are attributed

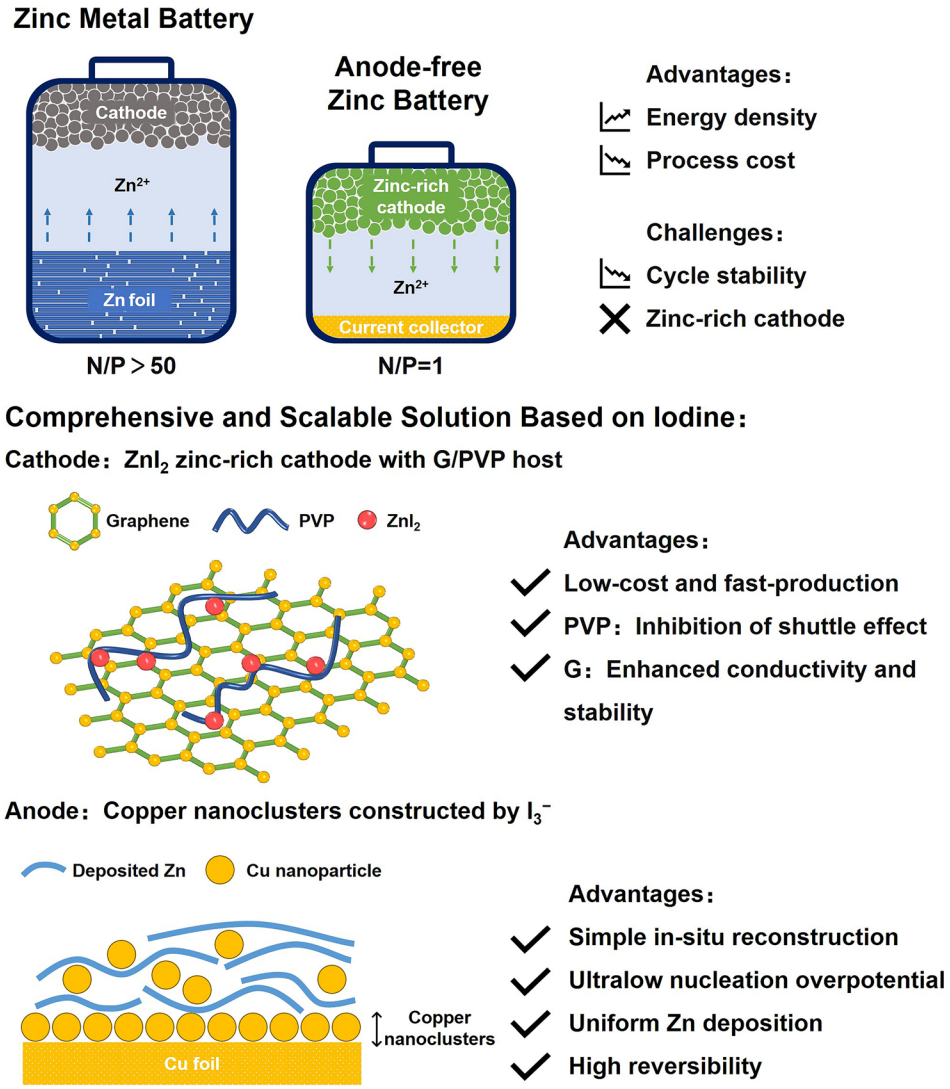

Fig. 1 Advantages and challenges for anode-free Zn metal batteries and the comprehensive solution based on iodine proposed in this work

to the (111) and (220) crystal planes of CuI [27], respectively. The high-resolution XPS spectra verified the strong $Cu^{1+}2p_{3/2}$ (932.3 eV) and $Cu^{1+}2p_{1/2}$ (932.3 eV) peaks [28] (Fig. S1), which also indicate the existence of CuI.

Next, in situ electrochemical reduction of the iodine-treated copper foil was performed in the Cu/Zn half cell. Notably, the open circuit potential of CuI/Zn half cell is reduced from 0.9 to 0.6 V compared to the untreated Cu/Zn half cell. According to previous reports, CuI, as a conversion electrode material, can undergo a reversible redox reaction with Zn^{2+} to generate Cu [27]. When discharging the cell at a current density of 1 mA cm^{-2}, the CuI/Zn half cell exhibits a significant discharge plateau in the voltage range of 0.4–0.5 V (Fig. 3a), which can attribute to the reduction of CuI. In order to demonstrate that the reduction products at − 0.1 V are Cu, the surface layer of I_3^- treated Cu foil was separated from the Cu substrate by transparent adhesive tape. In the XRD pattern (Fig. S2), the I_3^- treated surface Cu foil shows the standard CuI characteristic peaks. After the reduction to 0.1 V, the CuI characteristic peaks are replaced by the characteristic peaks of Cu, indicating the reduction from CuI to Cu. For comparison, no characteristic peaks are observed in the XRD pattern of the transparent adhesive tape from the bare Cu surface. In addition, the cyclic voltammetry (CV) curve (Fig. 2c) of the CuI-Zn half cell further confirms the electrochemical conversion between CuI and

 https://doi.org/10.1007/s40820-022-00948-9

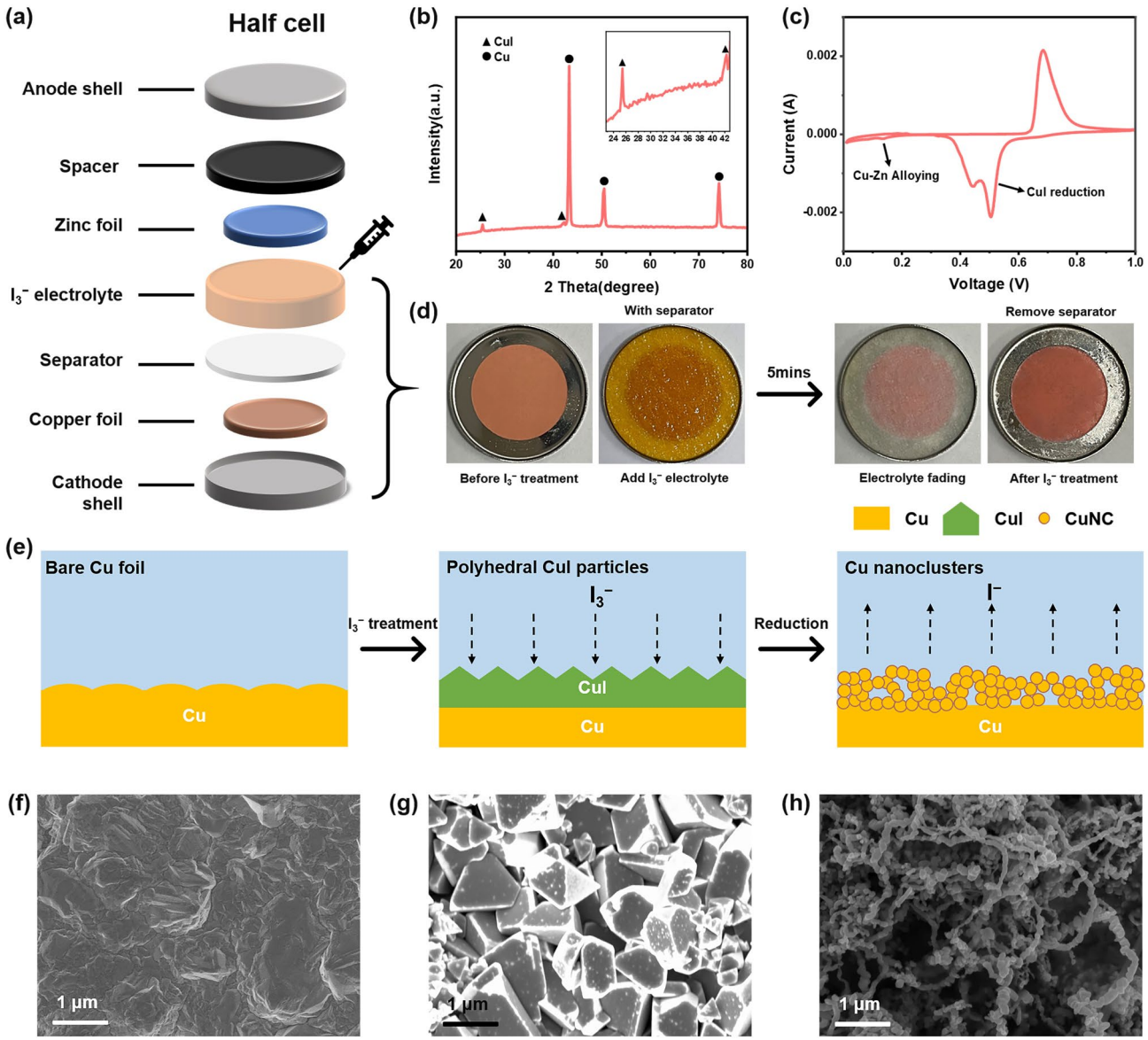

Fig. 2 **a** Schematic illustration of the assembly process of half cell. **b** XRD pattern of the iodine-treated Cu foil. **c** CV curves of the CuI-Zn half cell at 0.2 mV s^{-1} with the voltage range of 0.01–1 V. **d** Digital photographs of the reaction process between Cu foil and I_3^- electrolyte during the cell assembly process. **e** Schematic diagram of the surface morphological changes of the Cu foil during in situ reconstitution and the corresponding SEM images of Cu foil **f** before I_3^- treatment, **g** after I_3^- treatment and **h** after reduction to 0.1 V

Cu [29]. It is worth noting that the redox reaction of Cu to CuI occurs above 0.5 V, thus in order to ensure that Cu is no longer converted to CuI, the cutoff voltage is controlled below 0.5 V in the next half cell tests.

We next employed the *ex-situ* SEM characterization to visualize the evolution of the surface morphology of the Cu foil during iodine treatment (Fig. 2e). As shown in Figs. 2f–h and S3, the iodine-treated Cu foil changed from an intrinsically flat surface to a stack of micron-sized polyhedral particles. After the electrochemical reduction of CuI to 0.1 V, the micron-sized CuI particles were transformed into porous Cu nanoclusters (CuNCs). Actually, the electroreduction of CuI is an outside-in process [29]. Specifically, as shown in Fig. S4, due to the dense structure of CuI, Zn^{2+} can only react with the outer layer of CuI to generate loose Cu nanostructure on the surface, which allows Zn^{2+} to cross the outer layer and further reduce the inner layer of CuI. Thus, with the layer-by-layer reduction of CuI,

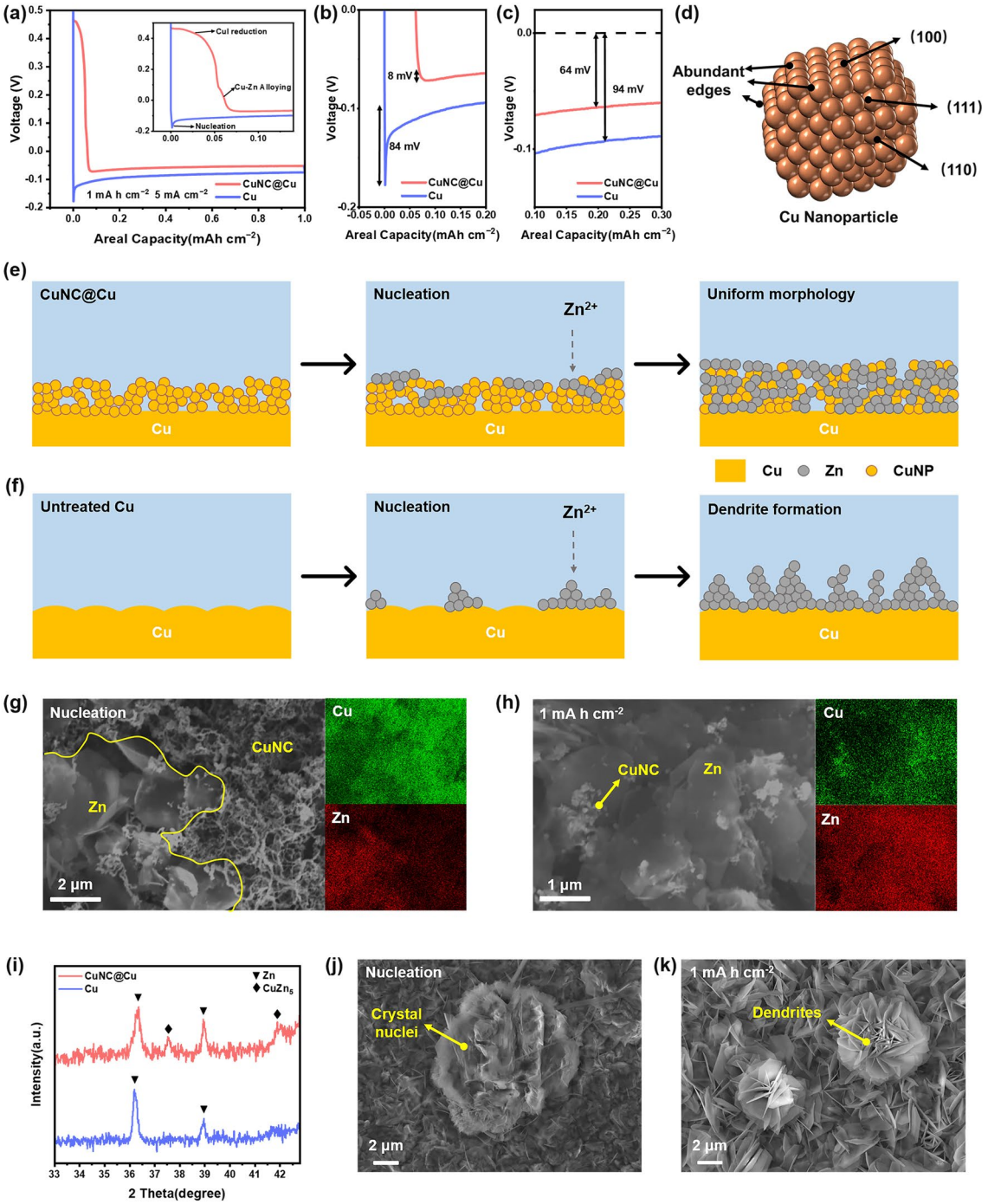

Fig. 3 **a** First-cycle galvanostatic deposition curve on CuNC@Cu and Cu electrodes at 5 mA cm^{-2}, and the inset shows the different deposition process of these two electrodes. Comparison of **b** nucleation overpotential and **c** deposition potential of CuNC@Cu and Cu electrodes at a current density of 5 mA cm^{-2}. **d** Schematic illustration of (100), (110), (111) planes and abundant facet edges of Cu nanoparticles. **e–f** Schematic illustrations of the Zn deposition behavior on CuNC@Cu and Cu electrodes. **g–h** SEM images and corresponding elemental mapping images of Zn deposition morphology on CuNC@Cu electrode at different deposition stages. **i** XRD patterns of CuNC@Cu and Cu electrode after deposition for 12 min. **j–k** SEM images of Zn deposition morphology on Cu electrode at different deposition stages

 https://doi.org/10.1007/s40820-022-00948-9

the CuI micron particles turn into loose Cu nanoclusters. Based on the above results, a nanostructured CuNC@Cu electrode is constructed by a simple in situ electrochemical reduction method.

3.2 Zn Deposition Behavior on CuNC@Cu Electrode

We then performed Zn deposition/dissolution tests and investigated the Zn deposition behavior by *ex-situ* XRD and SEM characterization in the CuNC@Cu/Zn half cells. For the CuNC@Cu electrode, a weak discharge capacity between 0 and 0.1 V is observed in the discharging curve (Fig. 3a). And such a discharge plateau consistently appears in subsequent cycles of CuNC@Cu/Zn half cells (Fig. S5). The corresponding redox peaks between 0 and 0.1 V can also be observed in the CV curve (Fig. 2c), which are attributed to the alloying and de-alloying processes of Cu and Zn [30]. In contrast, the voltage of the untreated Cu/Zn half-cell was instantaneously discharged to 0.01 V, without the alloying plateau. This is because compared to Cu foils, the Cu nanostructures with high specific surface area have more exposed edges of crystal planes in addition to the typical (100), (110), and (111) planes (Fig. 3d), and these edge sites have higher binding energy for Zn atoms [24], thus showing excellent zincophilic properties and lower alloying barrier with Zn [31, 32].

Zn deposition was performed at a current density of 5 mA cm^{-2}. For the untreated Cu electrode, a significant nucleation peak appears in the deposition curve with an overpotential as high as 84 mV. In contrast, on the CuNC@Cu electrode, the abundant zincophilic edge sites on CuNC and the formed Cu–Zn alloys can serve as nucleation sites, which greatly reduce the nucleation barriers, resulting in negligible Zn nucleation overpotential (8 mV) in the deposition curve of CuNC@Cu electrode (Fig. 3b). Furthermore, such an ultralow nucleation overpotential and alloying process are also observed in subsequent cycles (Fig. S6), indicating the stability of the CuNC@Cu structure and the reversible formation of Cu–Zn alloys. After nucleation, the Zn deposition morphology was observed by SEM. A large number of crystal nuclei appear on the surface of the untreated Cu electrode (Figs. 3j and S7), with Zn growing undirected around the crystal nuclei and accumulating as large dendrites. In contrast, for the CuNC@Cu electrode (Figs. 3g and S9a), due to a large number of exposed zincophilic sites and ample space for Zn deposition in the CuNC, Zn shows a flaky deposition morphology and horizontally lays on the surface of CuNC, and the corresponding elemental mapping images show the uniform distribution of Zn elements in the CuNC structure, indicating the co-existence of Cu–Zn alloy. The XRD pattern (Fig. S9b) also shows the characteristic peaks of Zn (002 plane at 36.2°) and $CuZn_5$ (42.0°), respectively. In addition, it is worthy to note that even in the stable Zn deposition stage, the deposition potential (Fig. 3c) of CuNC@Cu electrode (64 mV) is also significantly lower than that of the untreated Cu electrode (94 mV). And after stable deposition for 30 s, the Zn flakes further grow and uniformly cover the entire surface of CuNC (Fig. S10). After 12 min of deposition, with an area deposition capacity of 1 mAh cm^{-2}, the characteristic XRD peaks at 37.8° and 42° of $CuZn_5$ are detected on the CuNC@Cu electrode (Figs. 2i and S11d), which further confirm the continued alloying process of CuNC. Meanwhile, the SEM images and corresponding element mapping images (Figs. 2h and S12) show that the Zn flakes are not simply covered on the surface of CuNC, but a large number of Cu nanoparticles are dispersed between the Zn flakes, resulting in a horizontally stacked Zn/Cu composite structure. In contrast, no Cu–Zn alloys are observed in XRD pattern of the untreated Cu electrode (Figs. 2i and S8b). In its SEM images (Figs. 2k and S10a), Zn deposits as vertical blade-like dendrites and further gathers into large flower-like dendrites, which can result in dead Zn and short circuit of the cell.

The above results confirm that the CuNC@Cu electrode can achieve uniform Zn deposition with ultralow nucleation overpotential. In addition, as an important index to evaluate the reversibility and stability of the anode, we further tested the CE of the half cell. Under moderate conditions (1 mAh cm^{-2}, 5 mA cm^{-2}), the CuNC@Cu electrode can achieve an ultra-high average CE (ACE) of 99.88% with over 4000 stable cycles (1,700 h, Fig. 4a, c), while the untreated Cu electrode short out at 303rd cycle (Figs. 4b and S13), with an ACE of 99.14%. At higher current densities (1 mAh cm^{-2}, 20 mA cm^{-2}), the CuNC@Cu electrode delivers even better performance, achieving an ACE of 99.91% over 7,000 steady cycles (800 h, Fig. S14), while the untreated Cu electrode shows 132 stable cycles, with an ACE of 99.42%. The excellent Zn deposition/dissolution reversibility and stability of CuNC@Cu electrode are superior compared with most of

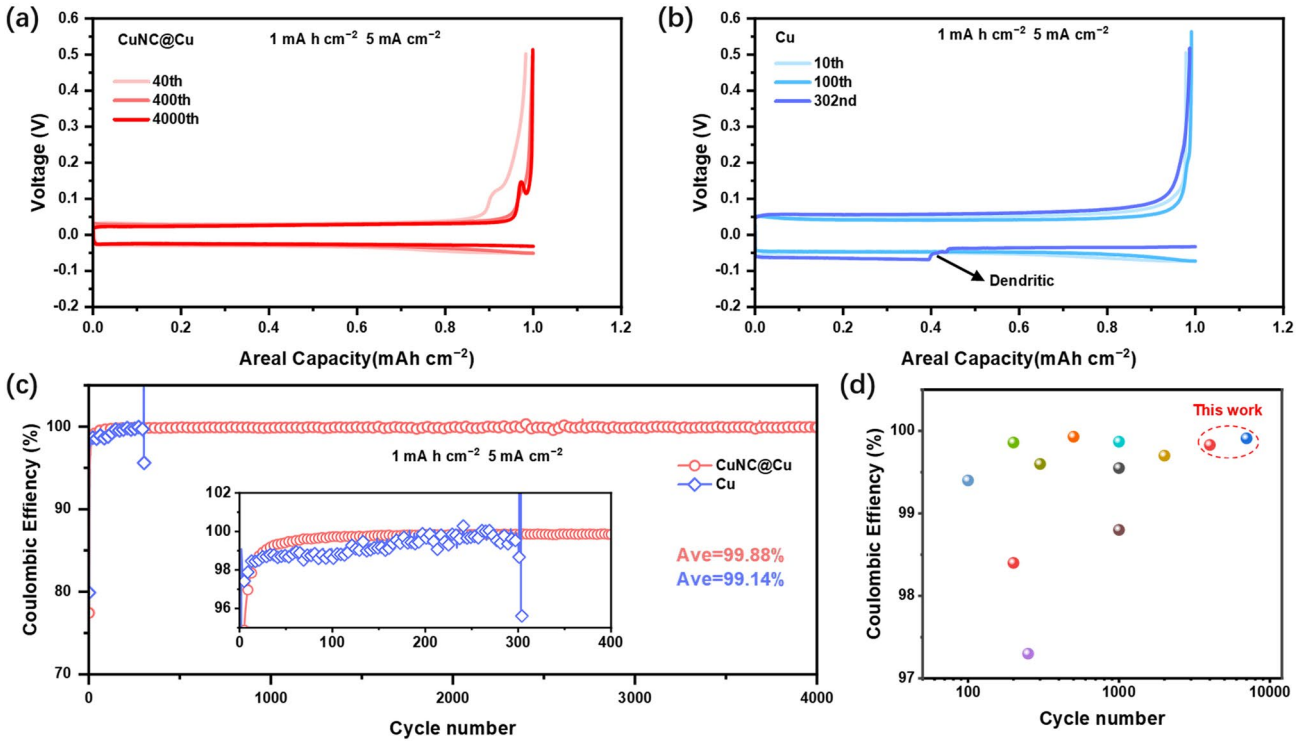

Fig. 4 Galvanostatic Zn deposition/dissolution curves of **a** CuNC@Cu and **b** Cu electrodes at selected cycles. **c** CE of Zn deposition/dissolution on CuNC@Cu and Cu electrodes at moderate conditions (1 mAh cm^{-2} and 5 mA cm^{-2}). **d** Comparison of ACE and cycle stability of this work with recently reported Zn half cells

the reported studies (Fig. 4d and Table S1) [8, 9, 12, 13, 16, 17, 33–36].

3.3 High-Performance Zn-rich Cathode

Another challenge for anode-free batteries is the lack of high-performance Zn-rich cathodes. For ZnI_2 cathode, the unique energy storage mechanism based on conversion reaction can provide sufficient Zn^{2+} ions for the anode. However, similar to the iodine cathode [37], ZnI_2 cathode is suffering from the shuttle effect of iodine species [38], which can cause severe self-discharge and iodine loss, resulting in low CE and dramatic capacity decay[39]. Meanwhile, the poor electronic conductivity of ZnI_2 greatly limits the utilization of iodine and increases the voltage polarization [40]. To address these issues, we propose a G/PVP heterogeneous structure as a host material for ZnI_2 cathode.

On the one hand, the strong $\pi-\pi$ interaction between G and PVP contributes to the homogeneous and stable structure of G/PVP [41]. PVP can significantly enhance the dispersibility of G in deionized water, therefore, G/PVP exhibits stable and homogeneous dispersion both before and after ultrasonic dispersion, while pure G is heavily aggregated (Fig. S15). Besides, in the SEM images of G/PVP@ZnI_2 cathode material (Figs. 5a and S16), no flocculent PVP is observed, while the corresponding element mapping image shows the uniform nitrogen distribution of PVP on the graphene surface. This evidence further demonstrates the homogeneous structure of G/PVP [42].Moreover, it is worth to note that, although PVP is water soluble, PVP with an average M_w of 30,000 used in this work is difficult to dissolve in the high concentration $ZnSO_4$ solution, as shown in Fig. S17a, the PVP solution in 2 M $ZnSO_4$ electrolyte is turbid compared to the clarified PVP aqueous solution. Similarly, when the G/PVP electrode was immersed in the 2 M $ZnSO_4$ electrolyte for 24 h, as shown in Fig. S17b, the PVP absorption peaks of G/PVP in the UV–vis spectra are negligible compared with the strong absorption peaks of the aqueous solution with the same mass of PVP, indicating that PVP is difficult to dissolve from the G/PVP electrode.

https://doi.org/10.1007/s40820-022-00948-9

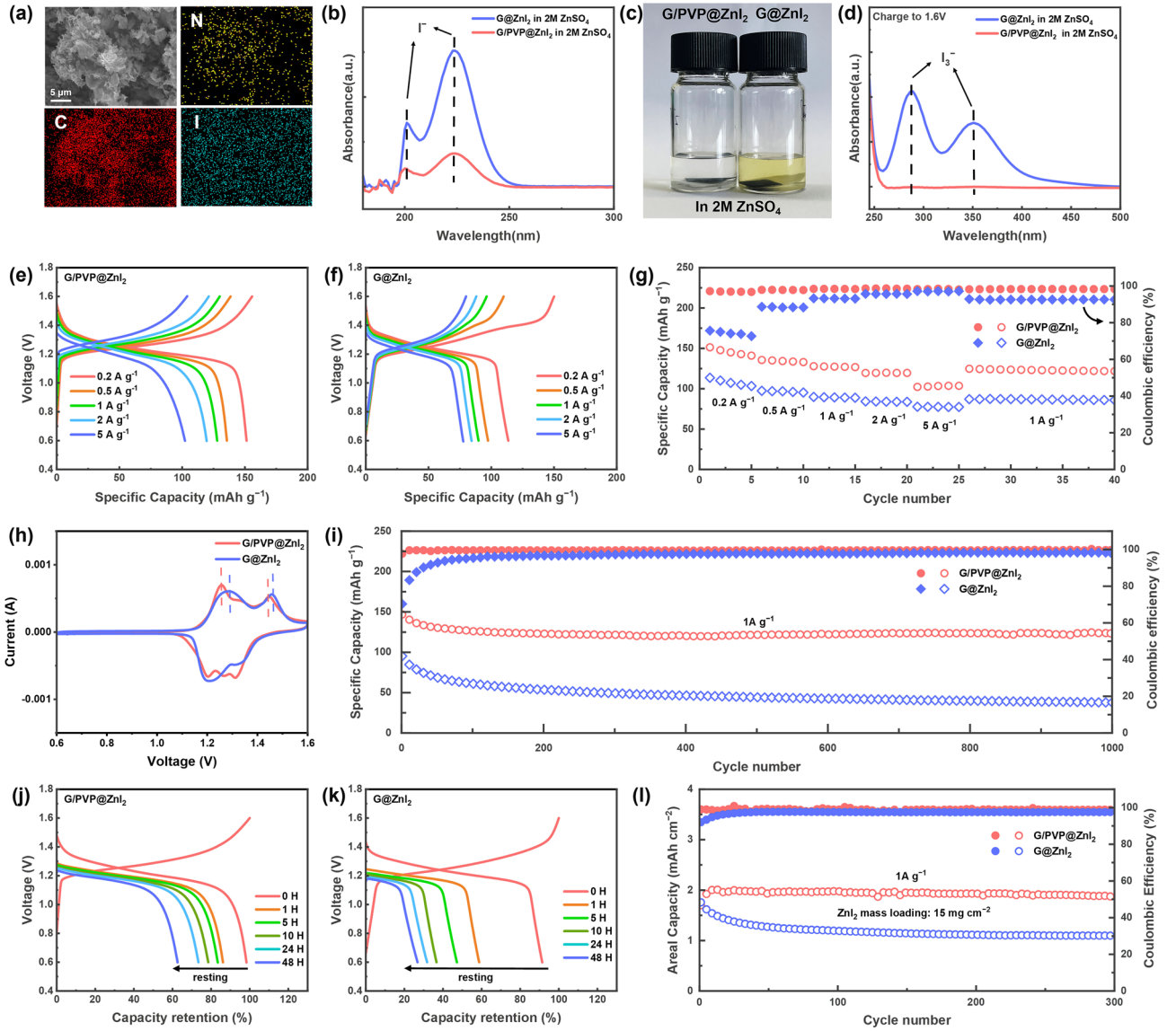

Fig. 5 **a** SEM image and corresponding elemental mapping images of G/PVP@ZnI_2 cathode material. **b** UV–vis absorption spectra of the $ZnSO_4$ electrolyte after immersing the G/PVP@ZnI_2 or G@ZnI_2 cathode for 24 h (both are diluted by 100 times). **c** Digital photographs of the color change of the $ZnSO_4$ electrolyte after immersing the full-charged G/PVP@ZnI_2/G@ZnI_2 cathode and separators for 24 h. **d** UV–vis absorption spectra of the $ZnSO_4$ electrolyte after immersing the full-charged G/PVP@ZnI_2 or G@ZnI_2 cathode for 24 h. **e–g** The rate performance and corresponding GDC curves of the G/PVP@ZnI_2 and G@ZnI_2 cathodes. **h** CV curves of the G/PVP@ZnI_2 and G@ZnI_2 cathodes at 0.2 mV s^{-1} with the voltage range of 0.6–1.6 V. **i** Long-term cycling test at 1 A g^{-1} of the G/PVP@ZnI_2 and G@ZnI_2 cathodes. **j–k** The self-discharge experiments of the G/PVP@ZnI_2 and G@ZnI_2 cathodes with a resting time of 0, 1, 5, 10, 24, and 48 h. **l** Cycling stability of the G/PVP@ZnI_2 and G@ZnI_2 cathodes at 1A g^{-1} under high areal mass loading

On the other hand, PVP can effectively inhibit the shuttle effect of iodine species, due to the strong electrostatic interaction between PVP and iodide ions. Specifically, PVP chains can form moderate hydrogen bonds with I_n^- ($n = 1$, 3, 5) [43, 44]. For example, after immersing the pre-cycle G/PVP@ZnI_2 cathode and G@ZnI_2 cathode in the 2 M $ZnSO_4$ electrolyte for 24 h, the UV–vis spectra (Fig. 5b) show that the electrolyte immersed with G/PVP@ZnI_2 cathode exhibits a significantly lower I^- absorption peak. More importantly, the hydrogen bonds get stronger as the number of iodine atoms increases, therefore, the desorption energy barrier of iodine monomers is significantly higher than the

adsorption energy barrier [43]. As a result, PVP can effectively inhibit the diffusion of polyiodide to the electrolyte, which is the main cause for the shuttle effect. Disassemble the cells of both cathodes after charging to 1.6 V, yellow iodine species are evident on the separator of the G@ZnI_2 cathode (Fig. S18), while the separator color of G/PVP@ZnI_2 cathode is much lighter. After immersing the two samples of cathodes and separators in 2 M $ZnSO_4$ electrolyte for 24 h, respectively, as shown in Fig. 5c, the electrolyte immersed with G@ZnI_2 cathode obviously turns yellow, and the corresponding UV–vis spectra confirm the presence of I_3^- in the electrolyte (Fig. 5d). For comparison, the electrolyte immersed with G/PVP@ZnI_2 cathode stays colorless and the corresponding UV–vis spectra show negligible I_3^- absorption peak.

Galvanostatic discharging/charging (GDC) tests further demonstrated the suppression of shuttle effect by G/PVP. Figure 5e–g shows the GDC curves and rate performance of G/PVP@ZnI_2 and G@ZnI_2 cathodes under various current densities. The CEs of G/PVP@ZnI_2 cathode is significantly higher than that of the G@ZnI_2 cathode. At a low current density of 0.2 A g^{-1}, G/PVP@ZnI_2 cathode can deliver an average CE of 96.9%, while the G@ZnI_2 cathode can only deliver an average CE of 77.2%. Such a low CE results from the severe shuttle effect of the G@ZnI_2 cathode [45], which is effectively suppressed by the G/PVP@ZnI_2 cathode. Therefore, the G/PVP@ZnI_2 cathode exhibits excellent rate performance, delivering an average capacity of 145.6, 137.3, 124.4, 119.6, and 103.1 mAh g^{-1} at 0.2, 0.5, 1, 2, and 5 A g^{-1}, respectively, while the G@ZnI_2 cathode can only deliver an average capacity of 107.8, 96.5, 89.3, 84.0, and 77.5 mAh g^{-1} at 0.2, 0.5, 1, 2, and 5 A g^{-1}, respectively. Besides, we also performed self-discharge experiments to demonstrate the suppression of self-discharge behavior by G/PVP. As shown in Fig. 5j–k, after resting for 0, 1, 5, 10, 24, and 48 h, the G/PVP@ZnI_2 cathode can deliver a capacity retention of 98%, 86%, 83%, 79%, 73%, and 63%, respectively. By contrast, the capacity retention of G@ZnI_2 cathode is only 91%, 58%, 47%, 37%, 32%, and 27% after resting for 0, 1, 5, 10, 24, and 48 h, respectively. In addition, due to the excellent electronic conductivity and iodine affinity of G/PVP, lower charging voltage and polarization are shown in the charge/discharge curves of G/PVP@ZnI_2 cathode (Fig. S19). A similar voltage drop of the oxide peak is also observed in the CV curve (Fig. 5h).

In the long cycle test (Fig. 5i), the capacity retention rate of G/PVP@ZnI_2 cathode can reach 80% after 1,000 cycles, while the G@ZnI_2 cathode exhibits a sharp capacity decay, with less than 40% capacity retention after 1,000 cycles. In addition, because of the excellent conductivity and stability of G/PVP, we further increased the areal mass loading of cathode. At a high loading of 15 mg cm^{-2}, the cathode can deliver an area capacity of 2 mAh cm^{-2} (Fig. S20). Thereafter, no significant capacity decay was observed during 300 stable cycles (Fig. 5l). By contrast, the high mass loading G/PVP@ZnI_2 cathode shows rapid capacity decay, resulting in significantly lower area capacity. Such an outstanding high areal capacity performance of G/PVP@ZnI_2 cathode is highly important to increase the energy density of the full cell [46].

3.4 Electrochemical Performance of AFZIB

Based on the high-performance ZnI_2 cathode and the in situ reconstruction method for Cu anode (Fig. 6a), the AFZIB with G/PVP@ZnI_2 cathode and CuNC@Cu anode can deliver a specific capacity of 125.7 mAh g^{-1} at 1 A g^{-1} (Fig. 6c). It is worth to note that the I_3^- additive in the electrolyte delivers very limited capacity for AFZIB. As shown in Fig. S21, when assembling an AFZIB without ZnI_2 active substance in the cathode, it only delivers a capacity of about 1.6 mAh g^{-1} (based on the area mass loading of 15 mg cm^{-2}, which is the same as the normal AFZIB), which is only 1.3% of the normal AFZIB capacity.

The GDC curve of AFZIB (Fig. 6c–e) is similar to that of ZIB (Fig. 5e). However, as the capacity decays, the voltage inflection point in the discharge plateau becomes more and more forward, indicating that the capacity of AFZIB is mainly limited by the capacity of Zn. Consequently, due to the high reversibility of the CuNC@Cu electrode for Zn deposition/dissolution, AFZIB exhibits excellent cycling stability with a capacity retention of 63.8% after 200 cycles and an initial CE of 96.4% (Fig. 6f). While the capacity retention of AFZIB with G/PVP@ZnI_2 cathode and Cu anode is only 24.9% after 200 cycles, the capacity decays rapidly at the beginning of the cycle due to the quick loss of Zn, and the initial CE is only 83.8% (Fig. 6d). In the XRD pattern of the surface of Cu foil after cycling (separated from the Cu substrate by transparent adhesive tape, Fig. S22a), significant peak of zinc hydroxide by-product is observed.

https://doi.org/10.1007/s40820-022-00948-9

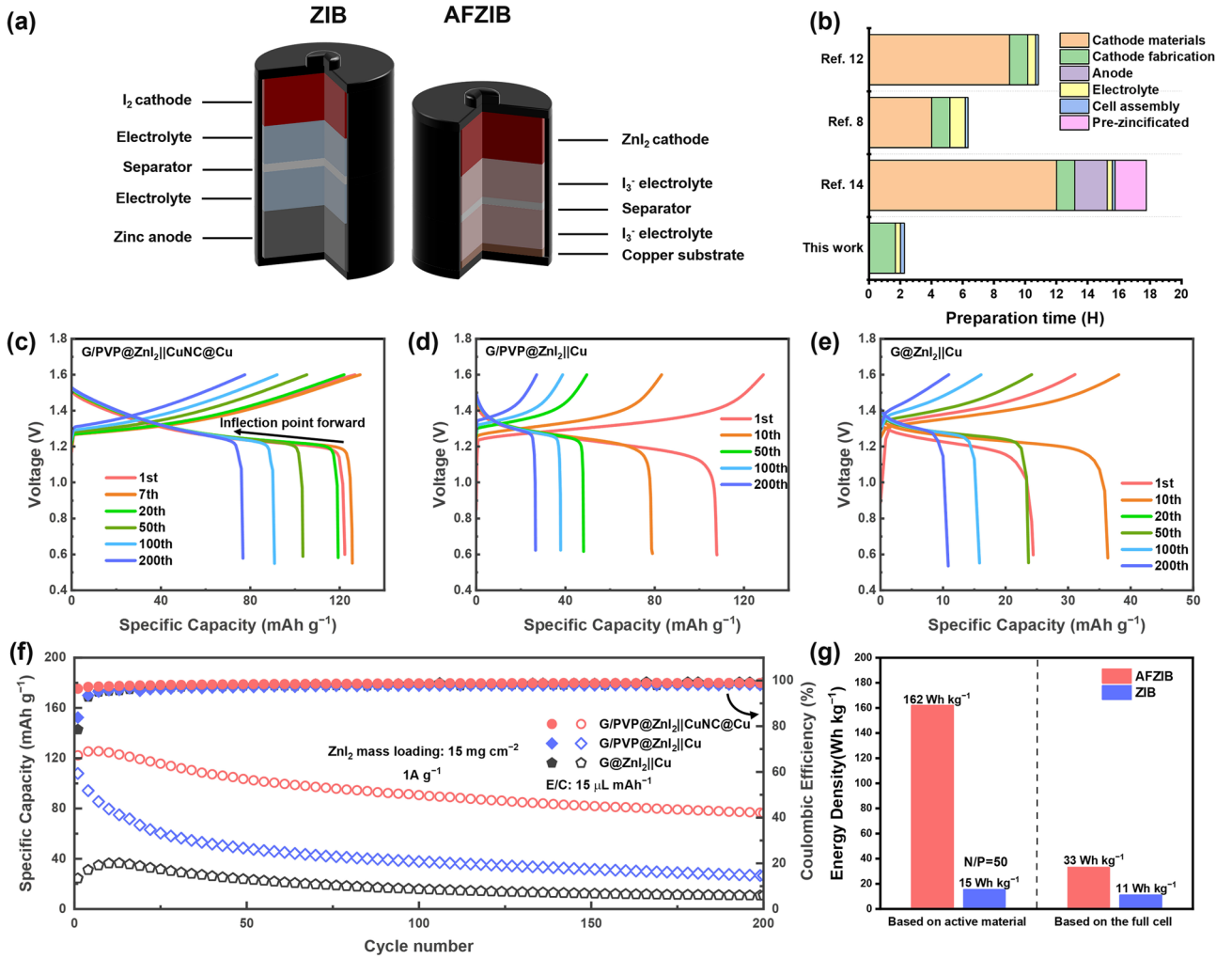

Fig. 6 **a** Schematic illustrations of the cell configurations of ZIB and AFZIB. **b** Comparison of preparation time of AFZIB and recently reported AFZBs. **c–e** GDC curves at 1 A g^{-1} of AFZIB with different battery configurations: **c** G/PVP@ZnI_2 cathode || CuNC@Cu anode, **d** G/PVP@ZnI_2 cathode || Cu anode, **e** G@ZnI_2 cathode || Cu anode. **f** Cycling stability of AFZIB at 1 A g^{-1} with different battery configurations. **g** Comparison of gravimetrical energy density of AFZIB and ZIB based on the mass of active material or the mass of full cell

Besides, if replacing the anode Cu foil with Zn foil after the significant capacity decay of G/PVP@ZnI_2||Cu battery, the cell capacity returns to the pre-decay level and performs stable cycling (Fig. S22b), which further demonstrates that the main reason for the capacity decay of AFZIB is the loss of Zn. Furthermore, when the cathode material is G@ZnI_2, due to the shuttle of active material and severe self-discharge, AFZIB can only deliver a capacity of 36.6 mAh g^{-1} and an initial CE of 78.6% (Fig. 6e), with a capacity retention rate of 29.5% for 200 cycles. Compared with recently reported AFZBs with cathode mass loading less than 2 mg cm^{-2}, our AFZIB exhibits superior performance even under high mass loading (15 mg cm^{-2}) and lean electrolyte (15 μL mAh^{-1}) conditions (Table S2). Such a close-to-practice condition is more informative when evaluating the commercialization potential of AFZBs.

More importantly, as the most prominent advantage of AFZIB (Fig. 6f), AFZIB can achieve a gravimetrical energy density of 162 Wh kg^{-1} (based on the total mass of active material), while the gravimetrical energy density of ZIB with 200 μm Zn foil anode is only 15 Wh kg^{-1}. Even when the mass of electrode hosts, electrolyte and separator are included in the calculation, the gravimetrical energy density of AFZIB can still reach 33 Wh kg^{-1}, which is three times higher than 11 Wh kg^{-1} of ZIB. In addition, commercial electrode materials and simple assembly processes in AFZIB

have obvious advantages. The total preparation and assembly process of AFZIB can be limited within 3 h (Fig. 6g), which is much faster than other reported AFZBs, thus reducing the cell production costs and enhancing the practical potential of AFZBs.

4 Conclusion

Together, we propose a comprehensive and scalable approach to promoting the electrochemical performance of AFZBs, where low-cost iodine plays an important role in overcoming both the anode and cathode issues. For the anode, the commercial Cu foil surface is in situ reconstructed into zincophilic Cu nanoclusters by I_3^- electrolyte additive. This nanocluster-structure achieves uniform Zn deposition with ultralow nucleation overpotential and high reversibility (average coulombic efficiency > 99.91% over 7,000 cycles). For the cathode, the unique conversion reaction-based energy storage mechanism of iodine enables the ZnI_2 cathode to provide sufficient Zn^{2+} for AFZB. Then, by optimizing the conductivity and suppressing the shuttle effect through a G/PVP cathode host, a high-capacity, cycling-stable Zn-rich cathode is obtained. Due to iodine enabled high performance of both electrodes, the assembled anode-free Zn iodine full cell delivers stable cycling (capacity retention of 63.8% after 200 cycles) and considerable energy density (162 Wh kg^{-1}) under a harsh condition of high cathode mass loading (15 mg cm^{-2}) and lean electrolyte addition (15 µL mAh^{-1}). More importantly, the low-cost electrode materials and fast-production process demonstrate the scale-up potential of AFZIB, which is crucial for the practical application of AFZBs.

Acknowledgements This work was financially supported by Shaanxi Yanchang Petroleum CO., Ltd (18529), Yiwu Research Institute of Fudan University (21557), the National Science Foundation of China (22075048), and the Shanghai International Collaboration Research Project (19520713900).

Funding Open access funding provided by Shanghai Jiao Tong University.

Supplementary Information The online version contains supplementary material available at https://doi.org/10.1007/s40820-022-00948-9.

References

1. G. Fang, J. Zhou, A. Pan, S. Liang, Recent advances in aqueous zinc-ion batteries. ACS Energy Lett. **3**(10), 2480–2501 (2018). https://doi.org/10.1021/acsenergylett.8b01426
2. M. Song, H. Tan, D. Chao, H.J. Fan, Recent advances in Zn-ion batteries. Adv. Funct. Mater. **28**(41), 1802564 (2018). https://doi.org/10.1002/adfm.201802564
3. X. Jia, C. Liu, Z.G. Neale, J. Yang, G. Cao, Active materials for aqueous zinc ion batteries: synthesis, crystal structure, morphology, and electrochemistry. Chem. Rev. **120**(15), 7795–7866 (2020). https://doi.org/10.1021/acs.chemrev.9b00628
4. J. Cao, D. Zhang, X. Zhang, Z. Zeng, J. Qin et al., Strategies of regulating Zn^{2+} solvation structures for dendrite-free and side reaction-suppressed zinc-ion batteries. Energy Environ. Sci. **15**(2), 499–528 (2022). https://doi.org/10.1039/d1ee03377h
5. L.E. Blanc, D. Kundu, L.F. Nazar, Scientific challenges for the implementation of Zn-ion batteries. Joule **4**(4), 771–799 (2020). https://doi.org/10.1016/j.joule.2020.03.002
6. B. Li, X. Zhang, T. Wang, Z. He, B. Lu et al., Interfacial engineering strategy for high-performance Zn metal anodes. Nano-Micro Lett. **14**, 6 (2021). https://doi.org/10.1007/s40820-021-00764-7
7. W. Du, S. Huang, Y. Zhang, M. Ye, C.C. Li, Enable commercial zinc powders for dendrite-free zinc anode with improved utilization rate by pristine graphene hybridization. Energy Storage Mater. **45**, 465–473 (2022). https://doi.org/10.1016/j.ensm.2021.12.007
8. C. Zhang, W. Shin, L. Zhu, C. Chen, J.C. Neuefeind et al., The electrolyte comprising more robust water and superhalides transforms Zn-metal anode reversibly and dendrite-free. Carbon Energy **3**(2), 339–348 (2020). https://doi.org/10.1002/cey2.70
9. F. Ming, Y. Zhu, G. Huang, A.H. Emwas, H. Liang et al., Co-solvent electrolyte engineering for stable anode-free zinc metal batteries. J. Am. Chem. Soc. **144**(16), 7160–7170 (2022). https://doi.org/10.1021/jacs.1c12764
10. W. Yao, P. Zou, M. Wang, H. Zhan, F. Kang et al., Design principle, optimization strategies, and future perspectives of anode-free configurations for high-energy rechargeable metal

batteries. Electrochem. Energy Rev. **4**(3), 601–631 (2021). https://doi.org/10.1007/s41918-021-00106-6

11. Y. Li, L. Wu, C. Dong, X. Wang, Y. Dong et al., Manipulating horizontal Zn deposition with graphene interpenetrated Zn hybrid foils for dendrite-free aqueous zinc ion batteries. Energy Environ. Mater. (2022). https://doi.org/10.1002/eem2.12423
12. Y. Zeng, P.X. Sun, Z. Pei, Q. Jin, X. Zhang et al., Nitrogen-doped carbon fibers embedded with zincophilic cu nanoboxes for stable Zn-metal anodes. Adv. Mater. **34**(18), e2200342 (2022). https://doi.org/10.1002/adma.202200342
13. Y. An, Y. Tian, K. Zhang, Y. Liu, C. Liu et al., Stable aqueous anode-free zinc batteries enabled by interfacial engineering. Adv. Funct. Mater. **31**(26), 2101886 (2021). https://doi.org/10.1002/adfm.202101886
14. L. Lin, K. Qin, Y.S. Hu, H. Li, X. Huang et al., A better choice to achieve high volumetric energy density: anode-free lithium-metal batteries. Adv. Mater. **34**(23), e2110323 (2022). https://doi.org/10.1002/adma.202110323
15. J. Yang, B. Yin, Y. Sun, H. Pan, W. Sun et al., Zinc anode for mild aqueous zinc-ion batteries: challenges, strategies, and perspectives. Nano-Micro Lett. **14**, 42 (2022). https://doi.org/10.1007/s40820-021-00782-5
16. Y. Zhu, Y. Cui, H.N. Alshareef, An anode-free Zn-MnO_2 battery. Nano Lett. **21**(3), 1446–1453 (2021). https://doi.org/10.1021/acs.nanolett.0c04519
17. G. Wang, M. Zhu, G. Chen, Z. Qu, B. Kohn et al., An anode-free Zn-graphite battery. Adv. Mater. **34**(29), 2201957 (2022). https://doi.org/10.1002/adma.202201957
18. J.B. Goodenough, How we made the Li-ion rechargeable battery. Nat. Electron. **1**(3), 204–204 (2018). https://doi.org/10.1038/s41928-018-0048-6
19. J. Wu, Q. Kuang, K. Zhang, J. Feng, C. Huang et al., Spinel $Zn_3V_3O_8$: a high-capacity zinc supplied cathode for aqueous Zn-ion batteries. Energy Storage Mater. **41**, 297–309 (2021). https://doi.org/10.1016/j.ensm.2021.06.006
20. J.C. Knight, S. Therese, A. Manthiram, Chemical extraction of Zn from $ZnMn_2O_4$-based spinels. J. Mater. Chem. A **3**(42), 21077–21082 (2015). https://doi.org/10.1039/c5ta06482a
21. C. Pan, R.G. Nuzzo, A.A. Gewirth, $ZnAl_xCo_{2-x}O_4$ spinels as cathode materials for non-aqueous Zn batteries with an open circuit voltage of ≤2 V. Chem. Mater. **29**(21), 9351–9359 (2017). https://doi.org/10.1021/acs.chemmater.7b03340
22. J. Zhang, Q. Liu, Y. Ruan, S. Lin, K. Wang et al., Monolithic crystalline swelling of graphite oxide: a bridge to ultralarge graphene oxide with high scalability. Chem. Mater. **30**(6), 1888–1897 (2018). https://doi.org/10.1021/acs.chemmater.7b04458
23. Z. Cai, Y. Ou, J. Wang, R. Xiao, L. Fu et al., Chemically resistant Cu–Zn/Zn composite anode for long cycling aqueous batteries. Energy Storage Mater. **27**, 205–211 (2020). https://doi.org/10.1016/j.ensm.2020.01.032
24. S. Xie, Y. Li, X. Li, Y. Zhou, Z. Dang et al., Stable zinc anodes enabled by zincophilic Cu nanowire networks. Nano-Micro Lett. **14**, 39 (2021). https://doi.org/10.1007/s40820-021-00783-4
25. L. Zhou, F. Yang, S. Zeng, X. Gao, X. Liu et al., Zincophilic Cu sites induce dendrite-free Zn anodes for robust alkaline/neutral aqueous batteries. Adv. Funct. Mater. **32**(15), 2110829 (2021). https://doi.org/10.1002/adfm.202110829
26. S. Liu, W. Shang, Y. Yang, D. Kang, C. Li et al., Effects of I_3^- electrolyte additive on the electrochemical performance of Zn anodes and Zn/MnO_2 batteries. Batteries Supercaps **5**(1), 202100221 (2021). https://doi.org/10.1002/batt.202100221
27. J. Meng, Z. Yang, L. Chen, X. Zeng, H. Chen et al., The investigation on the electrochemical performance of CuI as cathode material for zinc storage. Electrochim. Acta **338**, 135915 (2020). https://doi.org/10.1016/j.electacta.2020.135915
28. T. Ghodselahi, M.A. Vesaghi, A. Shafiekhani, A. Baghizadeh, M. Lameii, XPS study of the Cu@Cu_2O core-shell nanoparticles. Appl. Surf. Sci. **255**(5), 2730–2734 (2008). https://doi.org/10.1016/j.apsusc.2008.08.110
29. J. Hao, L. Yuan, B. Johannessen, Y. Zhu, Y. Jiao et al., Studying the conversion mechanism to broaden cathode options in aqueous zinc-ion batteries. Angew. Chem. Int. Ed. **60**(47), 25114–25121 (2021). https://doi.org/10.1002/anie.202111398
30. Y. Zhang, J.D. Howe, S. Ben-Yoseph, Y. Wu, N. Liu, Unveiling the origin of alloy-seeded and nondendritic growth of Zn for rechargeable aqueous Zn batteries. ACS Energy Lett. **6**(2), 404–412 (2021). https://doi.org/10.1021/acsenergylett.0c02343
31. Q. Zhao, Y. Wang, W. Liu, X. Liu, H. Wang et al., An in-depth study of regulable zincophilic alloy matrix toward stable zinc metal batteries. Adv. Mater. Interfaces **9**(7), 2102254 (2022). https://doi.org/10.1002/admi.202102254
32. H. Meng, Q. Ran, T.Y. Dai, H. Shi, S.P. Zeng et al., Surface-alloyed nanoporous zinc as reversible and stable anodes for high-performance aqueous zinc-ion battery. Nano-Micro Lett. **14**, 128 (2022). https://doi.org/10.1007/s40820-022-00867-9
33. Z. Zhao, R. Wang, C. Peng, W. Chen, T. Wu et al., Horizontally arranged zinc platelet electrodeposits modulated by fluorinated covalent organic framework film for high-rate and durable aqueous zinc ion batteries. Nat. Commun. **12**, 6606 (2021). https://doi.org/10.1038/s41467-021-26947-9
34. J. Hao, X. Li, S. Zhang, F. Yang, X. Zeng et al., Designing dendrite-free zinc anodes for advanced aqueous zinc batteries. Adv. Funct. Mater. **30**(30), 2001263 (2020). https://doi.org/10.1002/adfm.202001263
35. X. Xie, S. Liang, J. Gao, S. Guo, J. Guo et al., Manipulating the ion-transfer kinetics and interface stability for high-performance zinc metal anodes. Energy Environ. Sci. **13**(2), 503–510 (2020). https://doi.org/10.1039/c9ee03545a
36. Z. Wang, J. Huang, Z. Guo, X. Dong, Y. Liu et al., A metal-organic framework host for highly reversible dendrite-free zinc metal anodes. Joule **3**(5), 1289–1300 (2019). https://doi.org/10.1016/j.joule.2019.02.012
37. X. Li, N. Li, Z. Huang, Z. Chen, G. Liang et al., Enhanced redox kinetics and duration of aqueous I_2/I^- conversion

chemistry by MXene confinement. Adv. Mater. **33**(8), 2006897 (2021). https://doi.org/10.1002/adma.202006897

38. J. Ma, M. Liu, Y. He, J. Zhang, Iodine redox chemistry in rechargeable batteries. Angew. Chem. Int. Ed. **60**(23), 12636–12647 (2021). https://doi.org/10.1002/anie.202009871
39. D. Lin, Y. Li, Recent advances of aqueous rechargeable zinc-iodine batteries: challenges, solutions, and prospects. Adv. Mater. **34**(23), 2108856 (2022). https://doi.org/10.1002/adma.202108856
40. Y. Yang, S. Liang, J. Zhou, Progress and prospect of the zinc–iodine battery. Curr. Opi. Electrochem. **30**, 100761 (2021). https://doi.org/10.1016/j.coelec.2021.100761
41. Y. Gu, Y. Sun, Y. Zhang, H. Chi, W. Zhang et al., Highly efficient adsorption of copper ions by a PVP-reduced graphene oxide based on a new adsorptions mechanism. Nano-Micro Lett. **6**, 80–87 (2014). https://doi.org/10.1007/bf03353772
42. Y. Wu, P. Deng, Y. Tian, J. Feng, J. Xiao et al., Simultaneous and sensitive determination of ascorbic acid, dopamine and uric acid via an electrochemical sensor based on PVP-graphene composite. J. Nanobiotechnol. **18**(1), 112 (2020). https://doi.org/10.1186/s12951-020-00672-9
43. H. Tian, S. Zhang, Z. Meng, W. He, W.Q. Han, Rechargeable aluminum/iodine battery redox chemistry in ionic liquid electrolyte. ACS Energy Lett. **2**(5), 1170–1176 (2017). https://doi.org/10.1021/acsenergylett.7b00160
44. R. Pažout, J. Housková, M. Dušek, J. Maixner, P. Kačer, Platinum precursor of anticancer drug: a structure fixed by long intermolecular N–H···I and C–H···I hydrogen bonds. Struct. Chem. **22**(6), 1325–1330 (2011). https://doi.org/10.1007/s11224-011-9826-8
45. Y. Zhang, D. Tao, F. Xu, T. Li, A low-cost and high-performance rechargeable magnesium battery based on povidone iodine cathode. Chem. Eng. J. **427**, 131592 (2022). https://doi.org/10.1016/j.cej.2021.131592
46. W. Shang, Q. Li, F. Jiang, B. Huang, J. Song, B. Zn et al., I_2 battery's performance by coating a zeolite-based cation-exchange protecting layer. Nano-Micro Lett. **14**, 82 (2022). https://doi.org/10.1007/s40820-022-00825-5

 https://doi.org/10.1007/s40820-022-00948-9